

Contents lists available at ScienceDirect

Journal of Membrane Science

journal homepage: www.elsevier.com/locate/memsci



Permeation dynamics of dimethyl methylphosphonate through polyelectrolyte composite membranes by in-situ Raman spectroscopy



Jonathan Colón-Ortiz, Pranav Ramesh, George Tsilomelekis, Alexander V. Neimark*

Department of Chemical and Biochemical Engineering, Rutgers University, Piscataway, NJ, USA

ARTICLE INFO

Keywords: Permeation of chemical warfare agent surrogates Polyelectrolyte composite membranes Chemical protection In-situ Raman spectroscopy ZnO nano-aggregates

ABSTRACT

Reliable measurement of permeability of membranes with respect of different chemical compounds is of paramount importance for the design of novel materials for selective separations, protective barriers against chemical warfare agents and toxic industrial chemicals. An original *in-situ* Raman spectroscopy experimental setup is devised to measure the dynamics of permeation of toxins with example of diffusion of dimethyl methylphosphonate (DMMP), a nerve agent surrogate, across polyelectrolyte composite membranes. Efficiency of the proposed method is demonstrated on two types of commercial membranes, Nafion 117 and Nexar MD9200, modified with metal oxide nanoparticles. It was found that loading membranes with ZnO nanoparticles significantly reduces agent permeation, enhancing its protective capabilities against hazardous substances. The proposed methodology can be adopted and applied for characterization of permeability of other types of CWAs, their simulants, and other chemicals through polymeric membranes of different origin.

1. Introduction

Protective materials against chemical warfare agents (CWAs), such as nuclear, biological and chemical (NBC) protective clothing, have been evolving from impermeable butyl rubber-based materials to permeable polyurethane foams mixed with activated carbon [1]. One of the challenges in designing protective wearable gear is the ability of the material to quickly permeate sweat and dissipate heat while blocking penetration of CWAs through the protective material. Earlier generations of NBC protective gear such as butyl rubber-based gloves, masks and boots, are excellent at blocking hazardous chemicals, since they are impermeable, but are not able to dissipate heat or sweat from the body causing serious heat strain [2]. As protective clothing technology evolved through time more protective features were included within textiles of military uniforms. An example of such technological development for chemical-biological (CB) protection includes the Joint Service Lightweight integrated Suit Technology (JSLIST), a multilayered air-permeable adsorptive textile, as it provides chemical protection, good mobility for the user, and heat stress reduction features [3]. An alternative approach encompasses the potential incorporation of secondary components, such as adsorbents or catalysts, where the hazardous substances can either selectively adsorb or decompose as they diffuse through the membranes respectively. Towards this, popular adsorbents like activated carbon are known for having substantially

large surface area to volume ratios of over 2600 m²g⁻¹, leading to adsorption capacities of over 950 mg of adsorbate per gram of adsorbent [4]. However, the hazardous substances were not decomposed remaining a threat even when trapped in activated charcoal until clothing was laundered [1]. Among alternative protective materials, polymer electrolyte membranes (PEM) have been considered as they possess breathability, selective permeability, and agent protective properties [5–7]. Understanding the behavior of CWAs through barriers enables the designer to devise clever ways to control or even enhance the protective properties of the materials involved in the protective material. Therefore, transport properties of CWAs through membrane or fabric systems are of paramount importance when designing protective clothing, as they determine the level of protection when exposed to these agents.

The properties of PEMs can be tailored by loading functional metaloxide nanoparticles (MONP) using the *in-situ* growth mechanism [8]. Growing MONP within PEM substrates allows for easy scalability for mass production as membranes go through very simple steps in order to incorporate inorganic catalysts. The incorporation of MONP within PEM substrates provide enhanced mechanical stability [9], along, as shown below, with the ability to hinder the permeation of harmful substances, thus providing chemical protection. In addition, the proposed alternative protective materials could have the potential to have self-decontaminating properties as CWAs could be decomposed by the

E-mail address: aneimark@rutgers.edu (A.V. Neimark).

^{*} Corresponding author.

nano-crystalline metal-oxides opening an opportunity towards recyclable garments.

In this study, we report a novel experimental setup to measure via in-situ Raman spectroscopy the membrane protective capabilities against harmful substances. As a practical example, we study the permeation of DMMP, a chemical warfare agent surrogate (CWS) for nerve agents, through composite MONP-PEM membranes. In-situ and in-operando Raman spectroscopy has become a powerful technique to study dynamic experiments, particularly those that require high sensitivity towards chemical and physical changes, such as changes in restructuring of metal-oxides during a chemical reaction [10,11], observing electrochemical changes in metal-oxides for charge storage applications [12], and monitoring reaction products during biomass conversion [13], as well as electrocatalytic water splitting reactions [14]. Moreover, in-situ Raman spectroscopy has been useful for monitoring liquid-phase kinetic phenomena such as functionalization of organic compounds for the production of urea-derivatives [15], measuring concentrations of CO₂ within water at high pressures [16], and real-time measurement of aqueous corrosion of borosilicate glass [17]. In-situ Raman spectroscopy measurements for permeation through membrane barriers have been also utilized for electrolytes [18,19].

Two sets of PEMs were used to assess their capabilities as protective materials, Nafion and Nexar. Nafion™ membranes, produced by DuPont, are part of a larger family of perfluorosulfonated ionomers (PFSI) that have been used in several applications such as proton exchange membrane fuel cells (PEMFCs) [20-22], super-acid catalysis [23,24], selective drying and humidification of gases [25,26], and chlor-alkali electrolysis [27,28]. Nafion membranes consist of a sulfonated tetrafluoroethylene (PTFE)-backbone that incorporate grafted perfluorovinyl ether groups terminated with sulfonate groups onto its PTFE backbone. Nafion shows great chemical stability to a vast amount of chemicals including very corrosive compounds such as hydrogen fluoride and hydrogen chloride gases. In addition, they present excellent mechanical and thermal stability thus making them ideal candidates for high temperature reactions in fuel cells [29,30] and particularly advantageous for chemical protection. Nafion 117 has an IEC of 0.91 meq/g, which yields in average polymer networks with 1100 equivalent weight (EW).

NEXAR® MD9200 membranes, produced by Kraton, are sulfonated penta-block copolymers comprised of styrene and ethylene-co-propylene blocks, where the central styrene block is sulfonated. They have been used in several applications such as alcohol dehydration [31,32], water purification [33], separation of solvents [34], nanofiltration [35], fuel cells [36], and for chemical protection [37]. These pentablock copolymers have been known to possess high water-vapor transmission rates, excellent mechanical and thermal stability [38] making them ideal for high performance clothing. Nexar has an ion exchange capacity (IEC) of 2.0 meq/g, which yields in average polymer networks with 500 equivalent weight (EW). The *in-situ* growth of MONP within PEM was performed as reported in our previous publication [8].

2. Experimental

2.1. Materials

Nafion-117 ionomer membranes with an equivalent weight of $1100~g/SO_3H$ were purchased from Ion Power, Inc. NEXAR® MD9200 solutions (11 wt% in Cyclohexane and Heptane) were obtained through Kraton. Salt reagents zinc nitrate hexahydrate (98%), and sodium hydroxide (> 97%) were purchased from Sigma-Aldrich.

2.2. Solvent casting of Nexar membranes

Nexar films were solvent-casted from NEXAR® MD9200 solutions (11 wt% in Cyclohexane and Heptane) using a mixture of 100 mL of tetrahydrofuran (THF) and 30 mL of NEXAR® MD9200 solution. The

polymer solution was thoroughly mixed for 6 h at room conditions. Afterwards, 25 mL of the solution was poured into 50 mL Teflon evaporation dishes and the dishes were covered with P2 filter paper (to help slow down the evaporation rate of solvent) and were left overnight at room conditions. After 3 days, Nexar films were slightly brown and about 500 μ m in thickness and were qualitatively robust and flexible.

2.3. In-situ growth of ZnO within polyelectrolyte membranes

Nexar and Nafion membranes were cut into 0.5 inch by 0.5 inch pieces and were immersed in HCl (1 M) at room conditions for 1 h to remove any impurities and then immersed in deionized (DI) water to remove any excess HCl from the previous step. Once washed, these membranes were labeled as "PEM-H+" where PEM represent either Nafion or Nexar. PEM-H+ membranes were immersed in 200 mL of 0.05 M Zn(NO₃)₂ solutions at room conditions for 1 h to allow for Zn²⁺ exchange and these samples were labeled "PEM-Zn²⁺". Afterwards, PEM-Zn²⁺ membranes were rinsed in DI water and immersed in 200 mL of 0.5 M NaOH at 60 °C for 1. This step allows for Zn²⁺ to hydrolyze and form Zn(OH)₂. Membranes were rinsed again in DI water and blotted dry before putting the membranes in an oven at 100 °C for 1 h. These samples were labeled "PEM-ZnO".

2.4. Physical characterization

X-Ray Diffraction (XRD). X-ray diffractograms were obtained using a Phillips XPert diffractometer (Bragg-Brentano geometry) with a CuK_α anode (1.5405 Å). The instrument was operated at 45 kV and 40 mA in a continuous scanning mode at a 0.02°/step acquisition rate with a dwell time of 2 s/step from 20 angles over the range of $10^\circ-90^\circ$ on a 20 scale using a 0.3 mm fixed receiving slit. Transmission Electron Microscopy (TEM). Transmission electron micrographs were obtained by a JEOL 1200EX electron microscope with AMT-XR41 digital camera with an accelerating voltage of 80 kV and 2-s sample exposure time. Samples were supported on lacey carbon type-A 300 mesh copper grids.

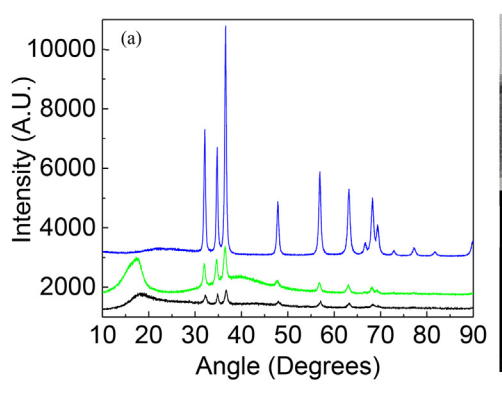
2.5. Spectroscopic characterization

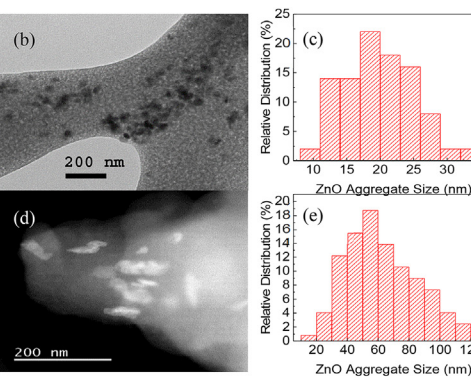
Raman spectra were acquired by using a Horiba LabRAM HR Evolution spectrometer with spectral resolution. The incident beam, which was a laser of 532 nm, and 80 mW initial power, was directed via a 90° macro lens of 40 mm focal length in the middle of the 2 ml vial that used to measure DMMP diffusion. The scattered light was collected through backscattering geometry and analyzed with an 1800gr/mm grating. Collection of the scattered light was achieved with an aircooled open electrode 1024x256 pixels CCD at the temperature of $-75\,^\circ\text{C}$. The acquisition time of each spectrum was 60–120secs, depending on the signal to noise (S/N) ratio and the number of accumulations varied in the range of 6–12. The spectral slit was fixed at $100\,\mu\text{m}$.

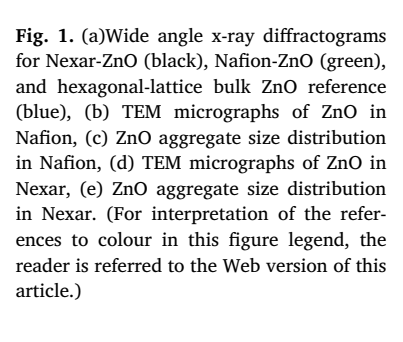
3. Results and discussion

3.1. Characterization of MONP-PEM composites

The samples were examined by x-ray diffraction (XRD) to confirm the presence of ZnO within the membranes. In Fig. 1(a), one can observe that Nafion and Nexar do have the characteristic peaks of hexagonal lattice ZnO as they match the superposed peaks of reference bulk ZnO. Once the presence of ZnO was confirmed by XRD, we apply transmission electron microscopy techniques in an effort to image and quantify the size of the ZnO nano-algregates within the Nexar substrates. Fig. 1(b,d) presents the ZnO nano-aggregates within PEM substrates. The ZnO nano-aggregate sizes range from 8 to 35 nm in Nafion-ZnO samples, Fig. 1(c). In the Nexar-ZnO samples, larger nanoaggregates with a wider distribution are observed with ZnO aggregate size







distributions that range from 10 to 120 nm, Fig. 1(e).

Although both PEM, Nafion and Nexar, were subjected to the same conditions for the in-situ growth of ZnO, there is a significant difference between the ZnO nanoaggregate size distributions. The polymer microstructure plays an important role during the nucleation and growth of ZnO nanocrystals. These membranes nano-segregate in such a way that the hydrophilic subphases, containing the sulfonate ions, coalesce and form interconnected channels that allow for water and ion transport upon hydration [39]. Since the nano-crystalline ZnO grow within the hydrophilic subphases of the membranes, the growth of such crystals may be limited by the confinement of the hydrophilic domains and the limited supply of Zn2+ ions available, which allow for nano-sized crystals to grow without a capping agent. It has been demonstrated that by using organic solvents, growth of ZnO within membranes can be manipulated to favor the growth of particular crystalline planes within ZnO.8It should be noted, since the studied Nafion and Nexar membranes have different microstructures and degrees of sulfonation, these may lead to the difference in ZnO aggregate size distributions.

3.2. DMMP permeation through MONP-PEM composites

A customized permeation setup, Fig. 2, was built to acquire *in-situ* Raman measurements of DMMP permeation through the PEM and PEM-MONP composites. The initial configuration comprises a 12 mL vial (top vial – donor compartment) with 10 mL of a 10 vol % solution of DMMP is connected to a 2 mL (bottom vial – receiving compartment) vial that filled by pure water. Both vials are separated by the PEM studied and were tightly sealed to avoid leakage from any compartment. 9 mm diameter samples of PEMs was utilized for all permeation experiments.

A 532 nm laser is used to radiate the small vial with water to detect the progression of DMMP permeation in the receiving compartment as a function of time. Fig. 3(a) shows the calibration set of spectra used to calculate the area under the curve (AUC) of the DMMP peak located at $715\,\mathrm{cm}^{-1}$, which is associated with its P–C stretching mode [(P–CH₃)] [40]. Fig. 3(b) shows a linear correlation with an R^2 of 0.999 over the entire range of DMMP concentrations studied.

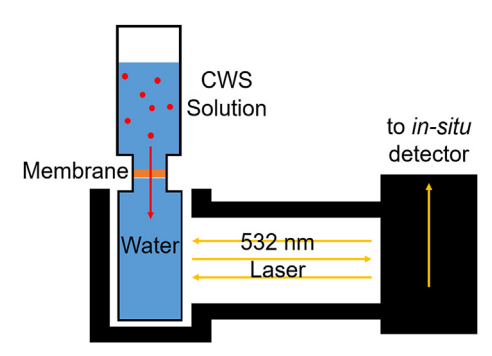


Fig. 2. Experimental in-situ Raman spectroscopy setup for permeation cell.

Once the calibration curve for DMMP in water was obtained, a series of spectra were collected for all permeation experiments against the different membranes studied, see Fig. 4.

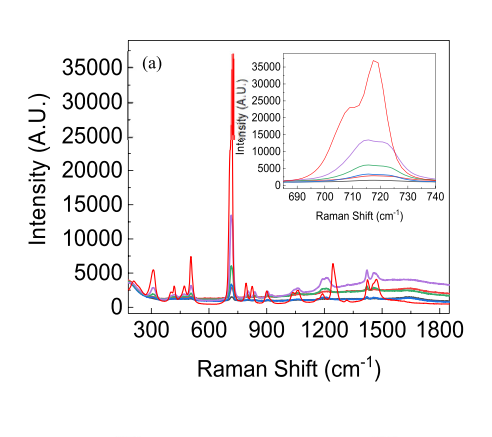
Full spectra from Fig. 4 was truncated within the wavenumber range of 615 and 825 cm⁻¹ to clearly observe the dynamics of the evolution of the DMMP peak located at 715 cm⁻¹ as a function of time as shown in Fig. 5. As it can be observed, the intensity of the peak at 715 cm⁻¹ after 1 h of permeation are most intense in the membranes without nanoparticles, Nafion-H⁺ and Nexar-H⁺, and is the peak intensity is significantly less with the ZnO incorporated membranes. It is evident that the incorporation of nanoparticles does have a great influence over the permeation rate of DMMP across the PEM, as it is seen on both Nafion and Nexar cases. It is possible that the additional ZnO-DMMP may hinder DMMP diffusion as ZnO serves as attractive centers from which DMMP may be strongly adsorbed to, as it has been reported previously, DMMP strongly adsorbs to metal-oxide surfaces [41]. The reduced Signal/noise ratio in some of our measurements is due to the combination of the low concentration as well as fast acquisition time. After performing a background subtraction and peak fitting for each spectra the AUC is calculated and later concentrations of permeated DMMP as a function of time are extracted from the calibration curve in Fig. 3(b).

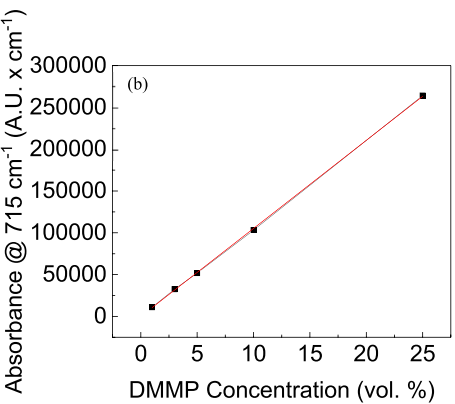
When plotting the permeated DMMP concentration on the receiving compartment as a function of time, as in Fig. 6(a), it can be seen that Nafion-H $^+$ has an observable breakthrough time, $t_{0,\ obs}$, defined as the time of the first observation of the non-zero concentration of DMMP in the receiving compartment, of 15 min when compared to Nafion-ZnO, which has a breakthrough time of 135 min, an order of magnitude longer. A similar increase of the breakthrough time upon addition of ZnO is found for Nexar samples, 45 and 145 min for Nexar-H $^+$ and Nexar-ZnO, respectively. In addition, the permeation rate of Nexar-H $^+$ is approximately 1.8, 2.3, and 3.8 times faster than Nafion-H $^+$, Nexar-ZnO, and Nafion-ZnO, respectively. These results show that the incorporation of ZnO nanoparticles has a large impact on both, breakthrough time and permeation rate in Nafion and Nexar samples, which demonstrates the enhancement in the protective capabilities that PEM-ZnO have against DMMP.

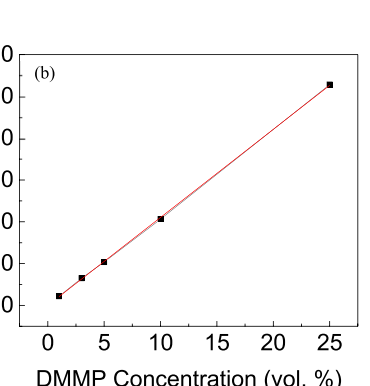
Fig. 6(a) shows that DMMP permeation through PEM can be analyzed by using a linear equation for diffusion in a plane sheet geometry [42].

$$C_B(t) = \frac{PC_AA}{V_BL}t\tag{1}$$

Equation (1) implies that $C_A \gg C_B$, where C_A and C_B are the DMMP concentrations in the donating and receiving compartments, respectively. L is the membrane thickness, A is the cross-sectional area of the membrane, and P is the permeability coefficient for DMMP. DMMP permeability, P is defined as the product DK, where D is the DMMP diffusion coefficient, and K is the partition coefficient (ratio of DMMP concentrations inside membrane and in the bulk solution at







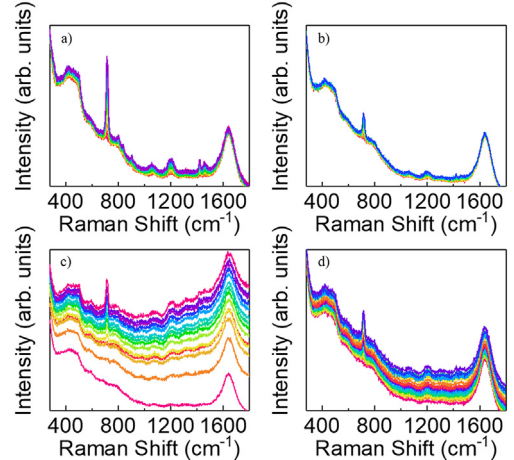


Fig. 4. Raman spectra of DMMP in the receiving compartment as a function of time through: (a) Nafion-H+, (b) Nafion-ZnO, (c) Nexar-H+, (d) Nexar-ZnO. Spectra collected every 30 min until 360 min, bottom to top spectra, respectively.

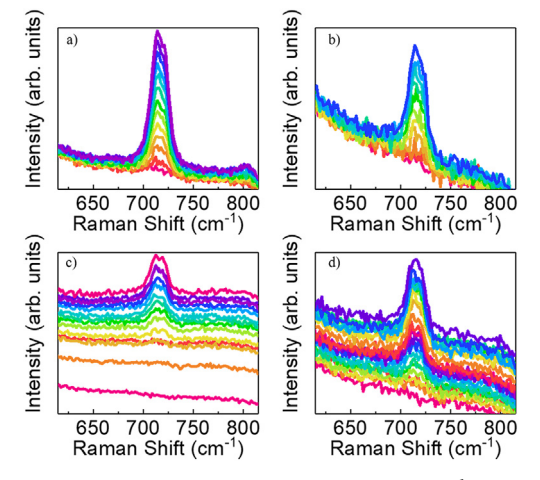


Fig. 5. DMMP spectral evolution at peak located at 715 cm⁻¹ as a function of time for DMMP permeation through: (a) Nafion-H⁺, (b) Nafion-ZnO, (c) Nexar-H⁺, (d) Nexar-ZnO.

equilibrium).

Data shown in Fig. 6(a) could be fit to by using Equation (1) and transport properties could be extracted. To compare membrane permeabilities across multiple samples, one has to account for the difference in the membrane thickness, approximately $190\,\mu m$ for Nafion and $500\,\mu m$ for Nexar. Rearranging Equation (1) into the following form below in Equation (2),

Fig. 3. (a) Raman spectra for DMMP samples in solutions of varying concentrations: (gray) 1 vol% DMMP, (orange) 3 vol% DMMP, (blue) 5 vol% DMMP, (green) 10 vol% DMMP, (violet) 25 vol% DMMP, (red) 100 vol% DMMP. Inset shows a closer look at DMMP peak at 715 cm⁻¹. (b) Calibration curve for DMMP based on Raman spectra. (For interpretation of the references to colour in this figure legend, the reader is referred to the Web version of this article.)

$$\frac{\Delta C_B(t)V_BL}{C_AA} = P(t - t_{0, obs})$$
(2)

provides a direct comparison between the sample permeabilities. Equation (2) presents the data shifted to the point, $t_{0, obs}$, of the first observation of a non-zero DMMP concentration in the receiving compartment and $\Delta C_B(t) = C_B(t) - C_B(t_{0, obs})$. The observed breakthrough times, $t_{0, obs}$, were obtained from Fig. 6(a). The permeation data in the shifted coordinates of Equation (2) is shown in Fig. 6(b). The slopes of the linear fits of permeation curves in Fig. 6(b) give the permeability constants, P. Linear fits of permeation curves in Fig. 6(b) had excellent agreement with an R² of 0.99, for the exception of Nexar-H⁺, which had an R² of 0.98.

Obtained transport parameters are given in Table 1. No reaction products were observed for DMMP within the time-frame and environmental conditions studied as DMMP is more stable than sarin given that it has a methyl group rather than the much more reactive fluorine that is present in sarin. However, the possibility of very small quantities of byproducts that fall below the detection limit of our Raman measurements cannot be excluded.

4. Conclusions

A novel in-situ Raman spectroscopy setup is built to measure agent permeation across protective barriers and applied to study DMMP permeation through ZnO loaded Nafion and Nexar polyelectrolyte membranes. It is shown that, incorporation of ZnO nanoparticles increases the breakthrough time and reduces the agent permeability, providing better protective capabilities of composite membranes. Of all samples studied, Nafion-ZnO seems to have the best protective capabilities against DMMP permeation. The proposed technique, which monitors the change of concentration in situ, as the permeation proceeds, has significant advantages compares to the existing methods for testing perm-selective membranes that are based on the measurements of permeants in the vapor phase that are transported to a detector by a flow of carrier gas. In-situ measurements provide high accuracy and require much shorter time due to a small sample cell. The proposed methodology can be adopted and applied for characterization of permeability of other types of CWAs, their simulants, and other chemicals through polymeric membranes of different origin.

Conflicts of interest

There are no conflicts to declare.

Acknowledgements

This work was supported by the Defense Threat Reduction Agency (DTRA) grant HDTRA1-14-1-0015, and the National Science Foundation Award #1705825. Authors would like to thank Dr. Carl

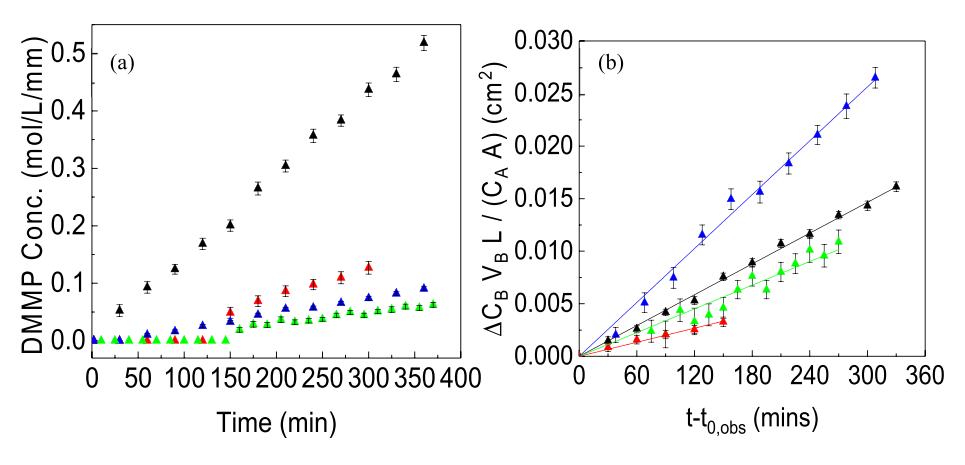


Fig. 6. (a) DMMP concentration in receiving compartment as a function of time, (b) Rearranged DMMP permeation as expressed in Equation (2): (black triangles) Nafion-H⁺, (red triangles) Nafion-ZnO, (blue triangles) Nexar-H⁺, and (green triangles) Nexar- ZnO. Error bars are based on standard deviation from duplicate experiments. (For interpretation of the references to colour in this figure legend, the reader is referred to the Web version of this article.)

Table 1
List of transport properties of DMMP across PEM studied.

	$P \text{ (cm}^2/\text{s)} \times 10^7$	$t_{0, obs}^{a}$ (min)
Nafion-H+	8.14	15
Nafion-ZnO	3.72	135
Nexar-H+	14.20	45
Nexar-ZnO	6.27	145

^a Measurements have an uncertainty of \pm 15 min.

Willis and Richard Blackwell from Kraton for providing the Nexar MD9200 samples.

References

- M. Boopathi, B. Singh, R. Vijayaraghavan, A review on nbc body protective clothing, Open Text. J. 1 (2008) 1–8.
- [2] Y. Heled, Y. Epstein, D.S. Moran, Heat strain attenuation while wearing NBC clothing: dry-ice vest compared to water spray, Aviat Space Envir Md 75 (5) (2004) 391–396.
- [3] Y.W. Lin, G.T. Jou, G.H. Lin, Y.C. Chang, T.F. Lai, The evaluation of thermal comfort for CB protective garments, in: I.B. Mekjavic, S.N. Kounalakis, N.A.S. Taylor (Eds.), International Conference on Environmental Ergonomics XII, Piran, Slovenia, Biomed, 2007, pp. 375–378.
- [4] M. Baysal, K. Bilge, B. Yilmaz, M. Papila, Y. Yurum, Preparation of high surface area activated carbon from waste-biomass of sunflower piths: kinetics and equilibrium studies on the dye removal, J Environ Chem Eng 6 (2) (2018) 1702–1713.
- [5] X. Lu, V. Nguyen, X. Zeng, B.J. Elliott, D.L. Gin, Selective rejection of a water-soluble nerve agent stimulant using a nanoporous lyotropic liquid crystal-butyl rubber vapor barrier material: evidence for a molecular size-discrimination mechanism, J. Membr. Sci. 318 (1–2) (2008) 397–404.
- [6] K.-H. Jung, B. Pourdeyhimi, X. Zhang, Chemical protection performance of polystyrene sulfonic acid-filled polypropylene nonwoven membranes, J. Membr. Sci. 362 (1–2) (2010) 137–142.
- [7] D. Rivin, G. Meermeier, N.S. Schneider, A. Vishnyakov, A.V. Neimark, Simultaneous transport of water and organic molecules through polyelectrolyte membranes, J. Phys. Chem. B 108 (26) (2004) 8900–8909.
- [8] J. Landers, J. Colon-Ortiz, K. Zong, A. Goswami, T. Asefa, A. Vishnyakov, A.V. Neimark, In situ growth and characterization of metal oxide nanoparticles within polyelectrolyte membranes, Angew. Chem. Int. Ed. 55 (38) (2016) 11522–11527.
- [9] M. Homayoonfal, M.R. Mehrnia, Y.M. Mojtahedi, A.F. Ismail, Effect of metal and metal oxide nanoparticle impregnation route on structure and liquid filtration performance of polymeric nanocomposite membranes: a comprehensive review, Desalin. Water Treat. 51 (16–18) (2013) 3295–3316.
- [10] W. Elliott, R. Salemmilani, S. Mubeen, C.D. Meinhart, G.D. Stucky, M. Moskovits, Changes in the structure of electrodeposited manganese oxide water oxidation catalysts revealed by in-operando Raman spectroscopy, J. Catal. 371 (2019) 287, 200
- [11] G. Tsilomelekis, S. Boghosian, Structural and vibrational properties of molybdena catalysts supported on alumina and zirconia studied by in situ Raman and FTIR spectroscopies combined with ¹⁸O/¹⁶O isotopic substitution, Catal. Today 158 (1–2) (2010) 146–155.
- [12] D. Chen, D. Ding, X. Li, G.H. Waller, X. Xiong, M.A. El-Sayed, M. Liu, Probing the charge storage mechanism of a pseudocapacitive MnO₂ electrode using in operando Raman spectroscopy, Chem. Mater. 27 (19) (2015) 6608–6619.
- [13] P. Ramesh, A. Kritikos, G. Tsilomelekis, Effect of metal chlorides on glucose mutarotation and possible implications on humin formation, React Chem Eng 4 (2) (2019) 273–277.

- [14] Y. Deng, B.S. Yeo, Characterization of electrocatalytic water splitting and CO₂ reduction reactions using in situ/operando Raman spectroscopy, ACS Catal. 7 (11) (2017) 7873–7889.
- [15] M. Tireli, M.J. Kulcsar, N. Cindro, D. Gracin, N. Biliskov, M. Borovina, M. Curic, I. Halasz, K. Uzarevic, Mechanochemical reactions studied by in situ Raman spectroscopy: base catalysis in liquid-assisted grinding, Chem. Commun. 51 (38) (2015) 8058–8061.
- [16] L.T. Geng, K. Qu, W.J. Lu, L. Jiang, I.M. Chou, In situ Raman spectroscopic study of the pressure effect on the concentration of CO₂ in water at hydrate-liquid water equilibrium up to 900 bar, Fluid Phase Equilib. 438 (2017) 37–43.
- [17] T. Geisler, L. Dohmen, C. Lenting, M.B.K. Fritzsche, Real-time in situ observations of reaction and transport phenomena during silicate glass corrosion by fluid-cell Raman spectroscopy, Nat. Mater. 18 (4) (2019) 342-+.
- [18] T. Yamanaka, H. Nakagawa, S. Tsubouchi, Y. Domi, T. Doi, T. Abe, Z. Ogumi, In situ Raman spectroscopic studies on concentration change of electrolyte salt in a lithium ion model battery with closely faced graphite composite and LiCoO₂ composite electrodes by using an ultrafine microprobe, Electrochim. Acta 234 (2017) 93–98.
- [19] T. Yamanaka, H. Nakagawa, S. Tsubouchi, Y. Domi, T. Doi, T. Abe, Z. Ogumi, In situ Raman spectroscopic studies on concentration of electrolyte salt in lithium-ion batteries by using ultrafine multifiber probes, ChemSusChem 10 (5) (2017) 855–861
- [20] K. Ketpang, B. Son, D. Lee, S. Shanmugam, Porous zirconium oxide nanotube modified nafion composite membrane for polymer electrolyte membrane fuel cells operated under dry conditions, J. Membr. Sci. 488 (2015) 154–165.
- [21] Y. Devrim, A. Albostan, Enhancement of pem fuel cell performance at higher temperatures and lower humidities by high performance membrane electrode assembly based on nafion/zeolite membrane, Int. J. Hydrogen Energy 40 (44) (2015) 15328–15335.
- [22] N. Wehkamp, M. Breitwieser, A. Buchler, M. Klingele, R. Zengerle, S. Thiele, Directly deposited nafion/TiO₂ composite membranes for high power medium temperature fuel cells, RSC Adv. 6 (29) (2016) 24261–24266.
- [23] E. Ponomareva, M.A. Lopez-Martinez, D. Wiggere, M.V. Morales, I. Melian-Cabrera, Novel reactivation allows effective reuse of nation (R) super-acid nano-catalyst, Appl. Catal. Gen. 569 (2019) 134–140.
- [24] S.Z. Liang, G.B. Hammond, B. Xu, Efficient hydration of alkynes through acid-assisted bronsted acid catalysis, Chem. Commun. 51 (5) (2015) 903–906.
- [25] Y. Peng, Z.F. Sui, Y.S. Zhang, T. Wang, P. Norris, W.P. Pan, The effect of moisture on particulate matter measurements in an ultra-low emission power plant, Fuel 238 (2019) 430–439.
- [26] M. Schalenbach, T. Hoefner, P. Paciok, M. Carmo, W. Lueke, D. Stolten, Gas permeation through nafion. Part 1: measurements, J. Phys. Chem. C 119 (45) (2015) 25145–25155.
- [27] M.G. Hosseini, P. Zardari, Oxygen depolarized cathode in advanced chlor-alkali cell with Pt-Ru nanoparticles as electro-catalyst: effect of process conditions and response surface methodology, Desalin. Water Treat. 84 (2017) 299–308.
- [28] F. Franco, J. Prior, S. Velizarov, A. Mendes, A systematic performance history analysis of a chlor-alkali membrane electrolyser under industrial operating conditions, Appl Sci-Basel 9 (2) (2019).
- [29] B.R. Matos, M.A. Dresch, E.I. Santiago, L.P.R. Moraes, D.J. Carastan, J. Schoenmaker, I.A. Velasco-Davalos, A. Ruediger, A.C. Tavares, F.C. Fonseca, Nafion membranes annealed at high temperature and controlled humidity: structure, conductivity, and fuel cell performance, Electrochim. Acta 196 (2016) 110–117.
- [30] J. Maiti, N. Kakati, S.P. Woo, Y.S. Yoon, Nafion® based hybrid composite membrane containing go and dihydrogen phosphate functionalized ionic liquid for high temperature polymer electrolyte membrane fuel cell, Compos. Sci. Technol. 155 (2018) 189–196.
- [31] G.M. Shi, J. Zuo, S.H. Tang, S. Wei, T.S. Chung, Layer-by-Layer (LbL) polyelectrolyte membrane with Nexar™ polymer as a polyanion for pervaporation dehydration of ethanol, Separ. Purif. Technol. 140 (2015) 13–22.
- [32] J. Zuo, G.M. Shi, S. Wei, T.S. Chung, The development of novel nexar block copolymer/ultem composite membranes for C₂-C₄ alcohols dehydration via pervaporation, ACS Appl. Mater. Interfaces 6 (16) (2014) 13874–13883.
- [33] J. Yeo, S.Y. Kim, S. Kim, D.Y. Ryu, T.H. Kim, M.J. Park, Mechanically and

- structurally robust sulfonated block copolymer membranes for water purification applications, Nanotechnology 23 (24) (2012) 245703.
- [34] P.H. Duong, T.S. Chung, S. Wei, L. Irish, Highly permeable double-skinned forward osmosis membranes for anti-fouling in the emulsified oil-water separation process, Environ. Sci. Technol. 48 (8) (2014) 4537–4545.
- [35] Z. Thong, G. Han, Y. Cui, J. Gao, T.S. Chung, S.Y. Chan, S. Wei, Novel nanofiltration membranes consisting of a sulfonated pentablock copolymer rejection layer for heavy metal removal, Environ. Sci. Technol. 48 (23) (2014) 13880–13887.
- [36] F. Huang, T.D. Largier, W. Zheng, C.J. Cornelius, Pentablock copolymer morphology dependent transport and its impact upon film swelling, proton conductivity, hydrogen fuel cell operation, vanadium flow battery function, and electroactive actuator performance, J. Membr. Sci. 545 (2018) 1–10.
- [37] N.S. Schneider, W.S. Zukas, N.L. Pomerantz, Effect of cation exchange on dimethyl methylphosphonate permeation kinetics in a pentablock hydrocarbon ionomer and a perfluorocarbon ionomer, Polymer 55 (1) (2014) 150–159.
- [38] F.H. Akhtar, H. Vovushua, L.F. Villalobos, R. Shevate, M. Kumar, S.P. Nunes,

- U. Schwingenschlögl, K.-V. Peinemann, Highways for water molecules: interplay between nanostructure and water vapor transport in block copolymer membranes, J. Membr. Sci. 572 (2019) 641–649.
- [39] A. Vishnyakov, A.V. Neimark, Self-assembly in nafion membranes upon hydration: water mobility and adsorption isotherms, J. Phys. Chem. B 118 (38) (2014) 11353–11364.
- [40] O. Ruiz-Pesante, L.C. Pacheco-Londoño, O.M. Primera-Pedrozo, W. Ortiz, Y.M. Soto-Feliciano, D.E. Nieves, M.L. Ramirez, S.P. Hernández-Rivera, In Detection of Simulants and Degradation Products of Chemical Warfare Agents by Vibrational Spectroscopy, Defense and Security Symposium, SPIE, 2007, p. 10.
- [41] J. Henych, P. Janoš, M. Kormunda, J. Tolasz, V. Štengl, Reactive adsorption of toxic organophosphates parathion methyl and DMMP on nanostructured Ti/Ge oxides and their composites, Arabian Journal of Chemistry (2016) 0–11, https://doi.org/ 10.1016/j.arabjc.2016.06.002 In press.
- [42] J. Crank, The Mathematics of Diffusion, 2 ed., Oxford University Press, 1975.